Chemical weathering detection in the periglacial landscapes of Maritime Antarctica: New approach using geophysical sensors, topographic variables and machine learning algorithms

Danilo César de Mello [a], Gustavo Vieira Veloso [a], Cassio Marques Moquedace [a],
Isabelle de Angeli Oliveira [a], Márcio Rocha Francelino [a], Fabio Soares de Oliveira [b],
José João Lelis Leal de Souza [a], Lucas Carvalho Gomes [d,*],
Carlos Ernesto Gonçalves Reynaud Schaefer [a], Elpídio Inácio Fernandes-Filho [a],
Edgar Batista de Medeiros Júnior [a], José Alexandre Melo Demattê [c]

[a] Department of Soil Science, Federal University of Viçosa, Brazil
[b] Department of Geography, Federal University of Minas Gerais, Brazil
[c] Department of Soil Science, "Luiz de Queiroz" College of Agriculture, University of São Paulo, Av. Pádua Dias, 11, CP 9, Piracicaba, SP 13418-900, Brazil
[d] Department of Agroecology, Aarhus University, Blichers Allé 20, 8830 Tjele, Denmark

ARTICLE INFO

ABSTRACT

The chemical weathering intensity in Antarctica is underestimated. As the chemical weathering intensity increases, hydrological, geochemical and geophysical changes occur in the different environmental spheres and at their interfaces through reactions and energy flows. Thus, once chemical weathering rates are understood and estimated, they can be used to predict and assess changes and trends in different environmental spheres. Few studies on the chemical weathering intensity have been performed in Antarctica. We used radiometric and magnetic properties associated with terrain attributes and the chemical degree of alteration of the igneous rock to model the chemical weathering intensity in Maritime Antarctica by using machine learning. Then, we related the chemical weathering intensity and geophysical variables with periglacial processes. To do this, gamma-spectrometric and magnetic readings were carried out using proximal-field sensors at 91 points located on different lithologies in a representative area of Maritime Antarctica. A qualitative analysis of chemical alteration for the different lithologies was carried out based on field observations and rock properties, and the levels of the chemical weathering degree were established. The geophysical data associated with terrain attributes were used as input data in the modeling of the weathering intensity. Then, the levels of the rock weathering degree were used as the "y" variable in the models. The results indicated that the C5.0 algorithm had the best performance in predicting the weathering intensity, and the most important variables were eTh, ^{40}K, ^{40}K/eTh, ^{40}K/eU, the magnetic susceptibility and terrain attributes. The contents of radionuclides and ferrimagnetic minerals in different lithologies, concomitantly with the intensity at which chemical weathering occurs, determine the contents of these elements. However, the stability and distribution of these elements in a cold periglacial environment are controlled by periglacial processes. The chemical weathering intensity prediction model using gamma-spectrometric and magnetic data matched the *in situ* estimate of the chemical degree of alteration of the rock. The pyritized andesites showed the highest intensities of weathering, followed by tuffites, diorites, andesitic basalts and basaltic andesites, and the lowest weathering intensity was shown by undifferentiated marine sediments. This work highlighted the suitability of using machine learning techniques and proximal-field sensor data to study the chemical weathering process on different rocks in these important and inhospitable areas of the cryosphere system.
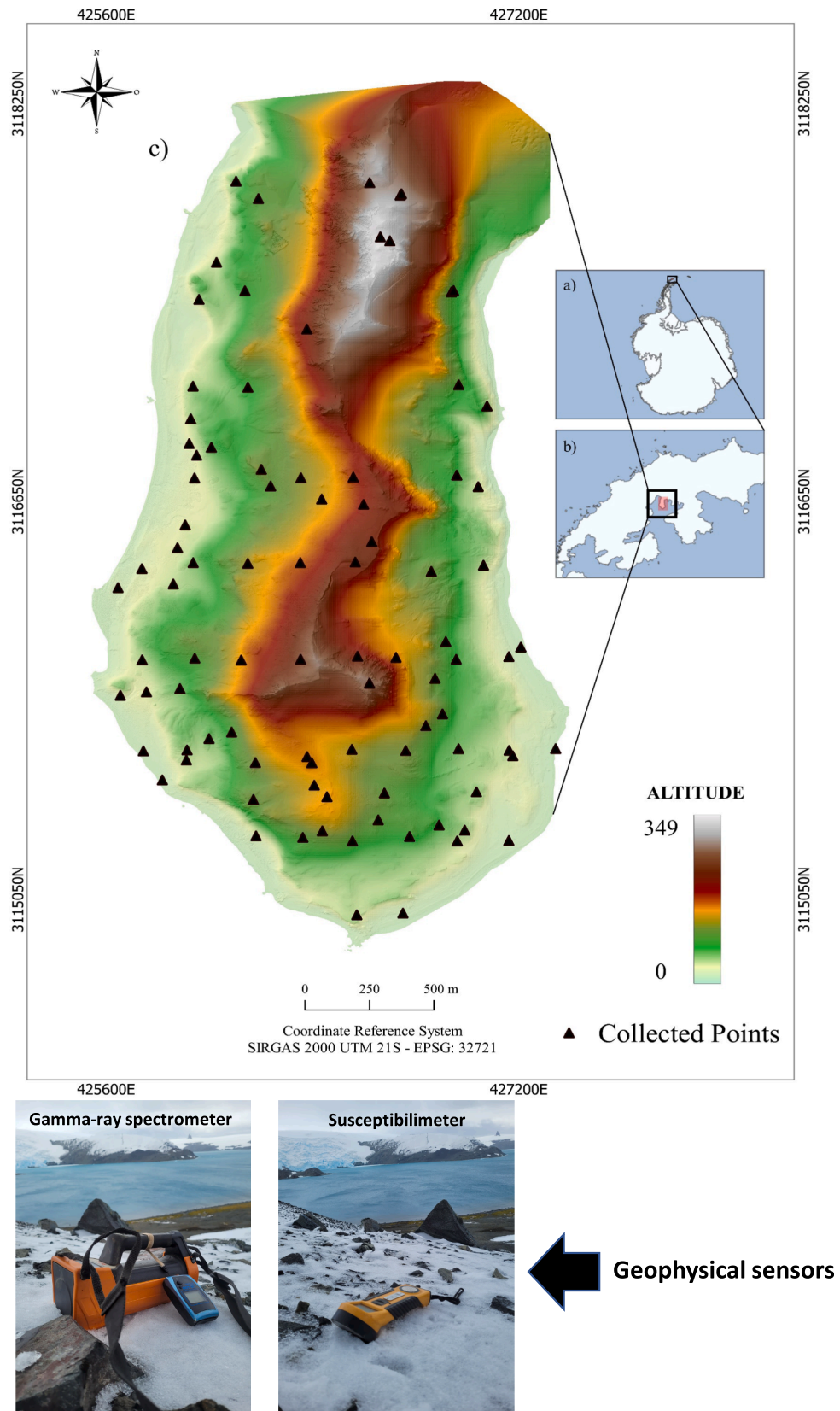

Fig. 1. Study area in Maritime Antarctica (Keller Peninsula), soil profiles, digital elevation model and geophysical sensors.

1. Introduction

Weathering processes comprises physical and chemical transformations in the lithosphere, in response to environmental factors such as the parent material, climate dynamics, topographic conditions, organisms and time (Carroll, 2012; Chesworth, 2008; Santos et al., 2019; White, 2018). Climate is an important marker of weathering conditions on a global scale, with higher rates of weathering occurring in hot, humid areas (Nahon, 1991). In the cold periglacial landscapes of Antarctica, such as those in Maritime Antarctica (MA), physical weathering predominates, mainly due to cryoclasty, although recent studies indicated that specific conditions lead to marked chemical weathering (Lopes et al., 2019; Schaefer et al., 2017; Siqueira et al., 2021; Lopes et al., 2022a). As a result, chemical weathering operates with a greater intensity in MA, when compared with the continental Antarctica (Lopes et al., 2019; Francelino et al., 2011; Simas et al., 2008). Under global warming, increases in chemical weathering rates are expected for the humid areas of Antarctica (Siegert et al., 2019).

Weathering studies can help us learn more about the types and variability of rock and soil attributes (Jenny, 1994; Scarciglia et al., 2005; Yoo et al., 2009), landscape evolution and geomorphic processes (Migoń, 2013a, 2013b; Turkington et al., 2005), chemical and mineralogical composition of rocks, soils and sediments (Jackson and Sherman, 1953; Prasetyo et al., 2016; Khelfaoui et al., 2020), potentially toxic elements (Yu et al., 2012; Cabral Pinto et al., 2017), biogeochemical cycles (Torres et al., 2016; Doetterl et al., 2018; Dynarski et al., 2019) and, the relationship between the pedosphere and other environmental spheres (hydrosphere, biosphere, lithosphere and atmosphere) (Buss et al., 2017) and climate change (Driese et al., 2021; Vicca et al., 2022).

The chemical-physical alteration of rocks exposed to different climatic conditions is a fundamental geomorphic process that can also be generally understood as "weathering." The chemical alterations of the rocks cause the weakening of the surface of the substrate, resulting in morphological features that reveal greater or lesser degrees of decomposition, disintegration or collapse (Hall et al., 2012).

Traditional non-destructive methods of evaluating the intensity of weathering of rocks, such as measuring the rock surface hardness and structure-from-motion have been widely used (e.g., Mol and Clarke, 2019). However, the emergence of new technologies has allowed the assessment of the weathering intensity of the rocks via remote and proximal sensors, with better spatial resolutions (Viles et al., 2011), making it possible to detect and quantify the weathering products resulting from the chemical alteration of rocks.

Geophysical techniques, such as gamma spectrometry and magnetic susceptibility, can improve and optimize studies involving the weathering degree and its relationships with the pedosphere and other environmental spheres (Beamish, 2013; McFadden and Scott, 2013; Mello et al., 2020; Mello et al., 2021; Mello et al., 2022; Reinhardt and Herrmann, 2019; Sarmast et al., 2017; Schuler et al., 2011). However, the degree of rock chemical weathering has hardly been investigated using this suite of techniques; the most pioneering work on this topic was undertaken in Australia continent by Wilford, (2012).

Proximal gamma-ray and magnetic susceptibility sensor are passive geophysical sensors. The gamma-ray spectrometer captures the energy released by the radionuclides potassium (^{40}K), equivalent uranium (eU^{238}) and equivalent thorium (eTh^{208}) directly in the soil, rocks and sediments (Wilford et al., 1997). The contents and distribution of these elements in the pedosphere, and their relationship with soil attributes were addressed by Mello et al. (2021) and Mello et al. (2022b), other studies addressed the relationship of these radionuclides with pedogenesis (Mello et al., 2022; Wilford et al., 2016) and weathering (de Mello et al., 2022a; Wilford and Minty, 2006; Wilford and Thomas, 2012).

The magnetic susceptibility (κ) is the degree to which a soil can be magnetized (Rochette et al., 1992) and, it is determined by the soil

mineralogy, parent material and presence of ferrimagnetic minerals, that is, mainly maghemite and magnetite (Ayoubi et al., 2018) but also others such as ferrihydrite and hematite (Valaee et al., 2016). In Fe-rich parent materials, the set of factors that determine the soil κ value are directly related to the weathering intensity (Mello et al., 2022; Mello et al., 2020), since the more weathered the soil, the greater the predominance of secondary ferrimagnetic minerals (Blundell et al., 2009).

Although these technologies are well established, they are not commonly used in combination in geoscience studies. In addition, few studies focused on weathering degree assessment in periglacial environments such as M.A. (Lopes et al., 2022b; Siqueira et al., 2021). Even gamma spectrometric and magnetic proximal surveys in Antarctica are scarce, and no work has yet been performed using combination of these technologies. On ice-free surfaces under warming periglacial environments, a reference for the initial stages of rock-soil weathering can be considered a baseline for future higher weathering rates due to global warming (Ruiz-Pereira et al., 2022).

Changes in the chemical and/or mineralogical composition of rocks can be used to assess the degree of chemical weathering. For example, geochemical weathering indices, based on the greater or lesser mobility of certain elements during weathering, have been successfully used to assess the degree of weathering of rocks (Chittleborough, 1991; Cristina Barbosa Guimarães et al., 2021; Price and Velbel, 2003). However, these geochemical indices have great limitations in terms of their spatial distribution in the landscape, and it may be useful to use a substitute (Wilford, 2012). In this paper, we used radionuclides and the magnetic susceptibility as substitute for traditional geochemical indices from proximal geophysical surveys, in combination with terrain attributes, to model the weathering intensity in M.A using machine learning algorithms.

Therefore, the aim of this study was to investigate the potential of geophysical variables (specifically gamma-radiometric and magnetic susceptibility measurements), along with terrain variables to estimate the intensity of the degree of chemical weathering in surface rocks. To achieve this, a machine learning approach was employed to generate a spatial prediction of the weathering intensity. By doing this, this study seeks to enhance our understanding of the factors that govern weathering processes within the context of a representative periglacial landscape.

We expected that gamma-ray spectrometry, the rock κ value and the relief associated with lithological characteristics related to the chemical weathering resistance/degree could be used to model the chemical weathering intensity in a periglacial environment in MA; the chemical weathering intensity should have a close relationship with pedogenesis and the periglacial landscape evolution.

2. Material and methods

2.1. Study area and rocks outcrop

The study area is located in MA, in the ice-free areas of Keller Peninsula (62°4′33″ S, 58°23′46″W), Admiralty Bay, King George Island, and the South Shetland Archipelago (Fig. 1). Keller Peninsula has an area of approximately 500 ha with a length of approximately 4 km in the north–south direction and a width of 2 km in the east–west direction (Francelino et al., 2011).

The climate is typical of Maritime Antarctica, but somewhat warmer (Rakusa-Suszczewski et al., 1993). The mean air temperatures vary between +1.6 °C during the summer (December–March) and −5.3 °C during the winter (June–September) (INPE, 2009). The mean annual precipitation is about 400 mm.

The Keller Peninsula is between 0 and 380 m above sea level, and its slopes are between 0 and 75% (relief classes ranging from flat to steep). The main geomorphological and cryogenic features of Keller Peninsula are moraines, protalus, inactive rock glaciers, uplifted marine terraces and felsenmeer, which developed under paraglacial and periglacial
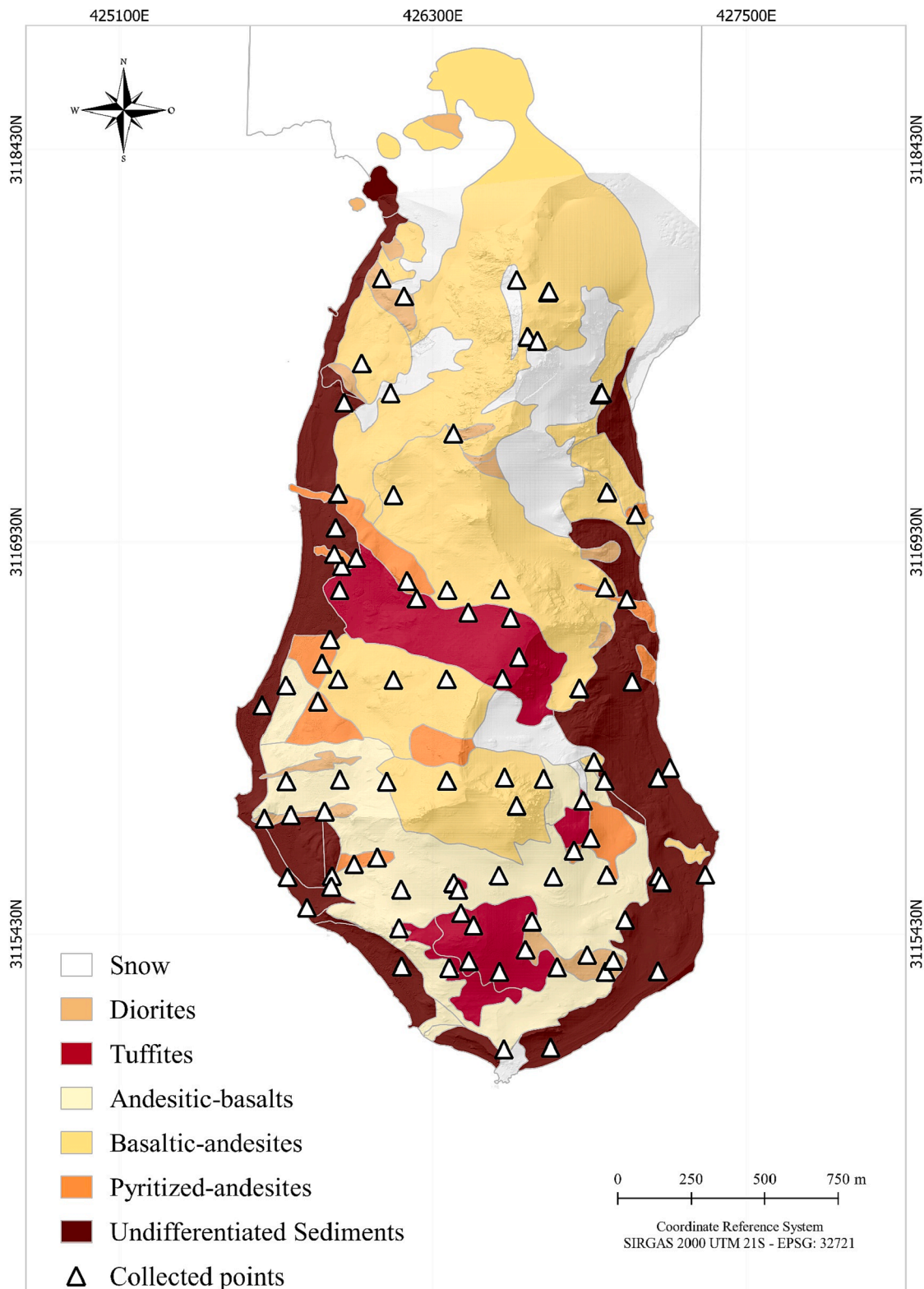
Fig. 2. Lithology and collected points. The lithological map was adapted from Francelino et al. (2011).

conditions (Francelino et al., 2011).

    The most detailed lithological map performed for Admiralty Bay and its vicinity was developed by British geologists based in a field station (Base G) on Keller Peninsula, between 1948 and 1960 (Birkenmajer, 1980), and it has a scale of 1:50000. The geological origin of the study area is associated with volcanic eruptions of transitional magmas between the oceanic crust and the Antarctic Plate that ranged from basaltic to andesitic lavas, with pyroclastic rocks, and volcanic tuffs, besides hypabyssal rocks, dated from the Upper Cretaceous to the Oligocene (Pride et al., 1990). In summary, the lithology of the Keller Peninsula is composed predominantly of igneous rock: andesitic-basalts, basaltic-andesites, diorites, pyritized-andesites, tuffites and

undifferentiated Quaternary deposits with mixed sediments (local rocks and rocks transported by marine erosion) (Fig. 2). Marine terraces occupy the lower parts of the landscape, and andesitic-basalts and basaltic-andesites occupy the upper parts of the landscape. The pyritized-andesites occupy varied positions in the landscape, while the tuffites are found at intermediate altitudes. Diorites are sporadic and more isolated in this area.

The grid of sample collection points where portable geophysical sensor readings was taken in the field (proximal gamma-ray and magnetic susceptibilimeter measurements) is shown in Fig. 1. The grid was established based on the variability of the lithology, associated with local toposequences, in a way that covered a representative area that contains all local lithologies.

2.2. Geophysical data collection

2.2.1. Magnetic susceptibility (κ) data

Surface readings of κ were recorded at all 91 points using a proximal geophysical susceptibility sensor (SC), Terraplus KT10 model (Fig. 1). This sensor can measure the soil κ value to a depth of 2 cm below the surface, with a precision of 10^{-6} SI units.

Soil κ readings were recorded with a proximal geophysical sensor, Terraplus KT10 model (Fig. 1), in scanner mode, which provides the most accurate reading values. This equipment is able to record magnetic susceptibility values up to 2 cm deep from the soil surface, with an accuracy of up to 10^{-6} SI. Readings were taken on the surface at the 91 points, shown in Fig. 1. Three readings were taken at each point and the average value of these readings was used in data processing. Finally, the soil κ data were concatenated with their respective physicochemical and gamma-ray spectrometric data for processing.

2.2.2. Gamma-ray spectrometric data

Gamma-spectrometric readings were performed with a proximal geophysical sensor (RS-230 model) (Solutions, 2009) (Fig. 1). This sensor quantifies the levels of the radionuclides equivalent uranium (eU in ppm), equivalent thorium (eTh in ppm) and potassium (^{40}K in %) in rocks, soils and sediments at a depths ranging from 30 to 60 cm, depending on the density and moisture of the substrate (Wilford et al., 1997; Taylor et al., 2002; Beamish, 2015). The values quantified in parts per million (*ppm*) and in as percentage (*%*) by the sensor were converted into units of mg kg^{-1} for data processing. This equipment has a portable GPS coupled with a 1 m precision for georeferencing the points.

First, the RS-230 sensor was properly calibrated according to the methodology of Grasty et al., (1991). Then, readings were performed in "essay mode", which provides greater precision, and the reading time was adjusted to 3 min at each point. Thus, the gamma spectrometric readings were taken on the substrate surface, at the 91 collection points shown in Fig. 1. Subsequently, the equipment data were transferred to a computer and concatenated with the soil κ values and the geology and physical–chemical data from the soil analysis.

The data from the geophysical sensors collected at the sampling points (gamma-ray spectrometric and magnetic susceptibility measurements) were spatialized using the minimum curvature function (Duval, 1990; McCafferty and Van Gosen, 2009), considering a resolution of 5 m. Spatialized gamma-spectroscopy maps (for eTh, eU and ^{40}K) were used to calculate the eTh/^{40}K and eU/^{40}K ratios.

2.3. Qualitative analyses of chemical weathering intensity

We analyzed the lithology (mainly rocks and their fragments) in ice-free areas according to a lithological map (1:50000 scale) and, assessed the surface radionuclides and κ values.

We proposed a qualitative analysis by creating six degrees of resistance for chemical weathering, considering the type of rocks and undifferentiated marine sediments; these values were used as the "*y*" variable in the weathering intensity prediction. The different degrees of

Table 1
Levels of the chemical weathering degree based on field observations of the alteration of the rocks and the characteristics of rocks (structure, texture and mineralogical composition).

Level	Degree of bedrock weathering	Rock chemical weathering resistance (literature)	Chemical degree of alteration of the rock (field observations)
1	Unweathered bedrock or not very weathered	Undifferentiated Sediments	Undifferentiated Sediments
2	Slightly weathered	Andesite - Basaltic	Andesite - Basaltics
3	Moderately weathered	Pyritized - Andesite	Basalt-Andesitics
4	Highly weathered	Basalt-Andesitic	Diorites
5	Very highly weathered	Diorite	Tuffites
6	Intensely weathered	Tuffites	Pyritized - Andesites

1 - The rock shows no sign and/or very little sign of chemical decomposition or staining. Bedrock predominates and/or an outcrop exceeds soil cover. Rocks without an apparent weathering pattern and/or difficult to identify weathering features or rock identity are present.
2 - The rock is slightly discolored. Overall, the bedrock fabric is very well preserved. The soils associated with the rocks are typically Regosols. Bedrock outcrops are common. The slight weathering of feldspars can be observed; the primary minerals are largely preserved. Coarse-textured igneous rocks are present and there is a higher occurrence of felsic minerals.
3 - The rock is more discolored. Residual gravel and coarse sands are common in the upper part of the weathering profile. The bedrock is partly decomposed but still cohesive, and mottling is common. Minor outcrops are present. Leptosols begin to appear. Igneous rocks of finer granulometry are present and ferro-magnesian mafic minerals are predominant.
4 – Saprock is common. Gravels and coarse sand content are common in the upper part of the rocks' weathered substrate. The bedrock structure and fabric are moderately preserved. A minor outcrop is present.
5 – Saprock and/or rock fragments are abundant and covered with silt and clay content in the upper part of the weathered saprock. Saprolite is moderately cohesive (it can be broken by pickaxe). Outcrops are present in low amounts and typically highly weathered. Medium-textured, porous rocks and easily decomposed minerals such as volcanic glass are present.
6 - Residual clays, silt and fine sand are common in the upper part of the rocks' weathered substrate. Saprolite is abundant and/or iron sulfide is common and evident. The edges of rocks and/or saprolites with an advanced and evident weathering front are visible. Usually there is no outcrop, and if an outcrop is present, it is typically very weathered and stained by iron oxides. A natural sulfurization process is evident.

resistance of materials to chemical weathering were established based on the following two factors: 1) the mineralogical composition, structure and texture of the rocks (Franke, 2009; Grotzinger and Jordan, 2013; Pye, 1986; Teixeira et al., 2009); and 2) the degrees of chemical alteration of the rocks, which was established based on field observations (supplementary material), by verifying the predominance or absence of features that indicate chemical weathering at a greater or lesser intensity, following the method of Wilford, (2012) (Table 1). However, due to the differences in the M.A. periglacial environment, we proposed an adaptation of this method.

Level 1 corresponds to a material with the highest degree of resistance to chemical weathering; in other words, this material will be the least weathered and less susceptible to chemical changes. On the other hand, level 6 corresponds to a material with the lowest degree of resistance to chemical weathering, and therefore, this material will be the most weathered and most susceptible to chemical alterations. Thus, there is a descending order of resistance of materials to chemical weathering from level 1 to level 6 (Table 1, "Rock chemical weathering resistance") and, an increasing order of degree of chemical alteration of materials from level one to level 6 (Table 1, "Chemical degree of alteration of the rock").

Table 2
Terrain attributes generated from the digital elevation model.

Terrain attributes	Abbreviations	Brief description
Aspect	AS	Slope orientation
Convergence index	CI	Convergence/divergence index in relation to runoff
Cross sectional curvature	CSC	Measures the curvature perpendicular to the down slope direction
Diurnal anisotropic heating	DAH	Continuous measurement of exposure dependent energy
Flow line curvature	FLC	Represents the projection of a gradient line onto a horizontal plane
General curvature	GC	The combination of both plan and profile curvatures
Hill	HI	Analytical hill shading
Hill index	HIINDEX	Analytical index hill shading
Longitudinal curvature	LC	Measures the curvature in the down slope direction
Maximal curvature	MAXC	Maximum curvature in local normal section
Mid-slope position	MSP	Represents the distance from the top to the valley, ranging from 0 to 1
Minimal curvature	MINC	Minimum curvature for local normal section
Morphometric Protection Index	MPI	Measure of exposure/protection of a point from the surrounding relief
Multiresolution index of ridge top flatness	MRRTF	Indicates flat positions in high altitude areas
Multiresolution index of valley bottom flatness	MRVBF	Indicates flat surfaces at the bottom of valley
Normalized height	NH	Vertical distance between base and ridge of normalized slope
Plan curvature	PLANC	Described as the curvature of the hypothetical contour line passing through a specific cell
Profile curvature	PROC	Describes surface curvature in the direction of the steepest incline
Real surface area	RSA	Actual calculation of cell area
Slope	S	Represents local angular slope
Slope height	SH	Vertical distance between base and ridge of slope
Slope Index	SI	Represents a local angular slope index
Solrad Diffuse1	SolDiffuse1	Diffuse insolation for the month of January
Solrad Diffuse2	SolDiffuse2	Diffuse insolation for the month of July
Solrad dur 1	SolDur1	Insolation duration for the month of January
Solrad dur 2	SolDur2	Insolation duration for the month of July
Solrad Direct1	SolDiret1	Direct insolation for the month of January
Solrad Direct2	SolDiret2	Direct insolation for the month of July
Solrad Ration1	SolRation1	Ratio between direct insolation and diffuse insolation for the month of January
Solrad Ration2	SolRation2	Ratio between direct insolation and diffuse insolation for the month of July
Solrad Sunrise1	SolSunrise1	Mean sunrise time for the month of January
Solrad Sunrise2	SolSunrise2	Mean sunrise time for the month of July
Solrad Sunset1	SolSunset1	Mean sunset time for the month of January
Solrad Sunset2	SolSunset2	Mean sunset time for the month of July
Solrad total1	SolTotal1	Total insolation for the month of January
Solrad total2	SolTotal2	Total insolation for the month of July
Standardized height	STANH	Vertical distance between base and standardized slope index
Surface specific points	SSP	Indicates differences between specific surface shift points

Table 2 (*continued*)

Terrain attributes	Abbreviations	Brief description
Tangential curvature	TANC	Measured in the normal plane in a direction perpendicular to the gradient
Terrain ruggedness index	TRI	Quantitative index of topography heterogeneity
Terrain surface convexity	TSC	Ratio of the number of cells that have positive curvature to the number of all valid cells within a specified search radius
Terrain surface texture	TST	Splits surface texture into 8, 12, or 16 classes
Total curvature	TC	General measure of surface curvature
Topographic position index	TPI	Difference between a point's elevation and surrounding elevation
Valley depth	VD	Calculation of vertical distance at drainage base level
Valley	VA	Calculation of fuzzy valley using the Top Hat approach
Valley Index	VA	Calculation of fuzzy valley index using the Top Hat approach
Vector ruggedness measure	VRM	Measures the variation in terrain roughness
Topographic wetness index	TWI	Describes the tendency of each cell to accumulate water as a function of relief

2.4. Digital elevation model and topographic attributes

The digital elevation model (DEM) (Fig. 1) was developed in the R software version 4.10 (R Core Team, 2022) using data from the digital terrain model (DTM), which consisted of a high-resolution topography survey (HRT). That survey was undertaken in 2014/2015 and 2015/2016 using a terrestrial laser scanner (TLS) (RIEGL VZ-1000 model), with a nominal accuracy and precision of 8 and 5 mm, respectively. This sensor and geoprocessing provided the elevated number of points per cell, resulting in a dense cloud of points. This dataset allowed the generalization process to obtain surface models with a high performance and provided the best representation of the local relief, allowing studies of landscape evolution on a micro scale in time, in which the pedogeo-morphological process can be assessed (Francelino et al., 2011).

Forty eight extra topographic attributes were created using the DEM data from the DTM (Table 2) using the *R* software (R Core Team, 2015), including the "*Rsaga*" (Brenning, 2008) and "*raster*" (Hijmans and Van Etten, 2016) packages (Table 2).

2.5. Selection of environmental covariates for modeling processes

For the prediction and spatialization of the chemical weathering intensity (CWI), eU, eTh, ^{40}K, κ, eTh/^{40}K, eU/^{40}K and relief topographic variables (derived from the DEM) were used as the "*x*" variables (input data) in the models. The chemical degree of alteration of the rock (six levels) was used as a the "*y*" variable in the modeling processes (outcome or dependent variable).

Four machine learning algorithms were tested; *C5.0, Random Forest* (RF), *Partial Least Squares* (pls), *k-Nearest Neighbors* (kknn). Three phases were used in the modeling processes: the selection of covariates, training/testing and spatialization. The general framework is illustrated in Fig. 3.

The selection of covariates was applied to reduces the complexity of the final model (parsimony) and, minimize the computational effort. In other words, here, highly correlated variables were removed to reduce information redundancy and make the model simpler (Gomes et al., 2019; Hasri et al., 2017; Seasholtz and Kowalski, 1993). This procedure is divided into three phases: (1) the removal of low-variance covariates (low variance/close to zero), (2) high correlation removal, and (3) selection according to the importance of the covariate (Mello et al., 2022b). These three phases are described in detail as follows:
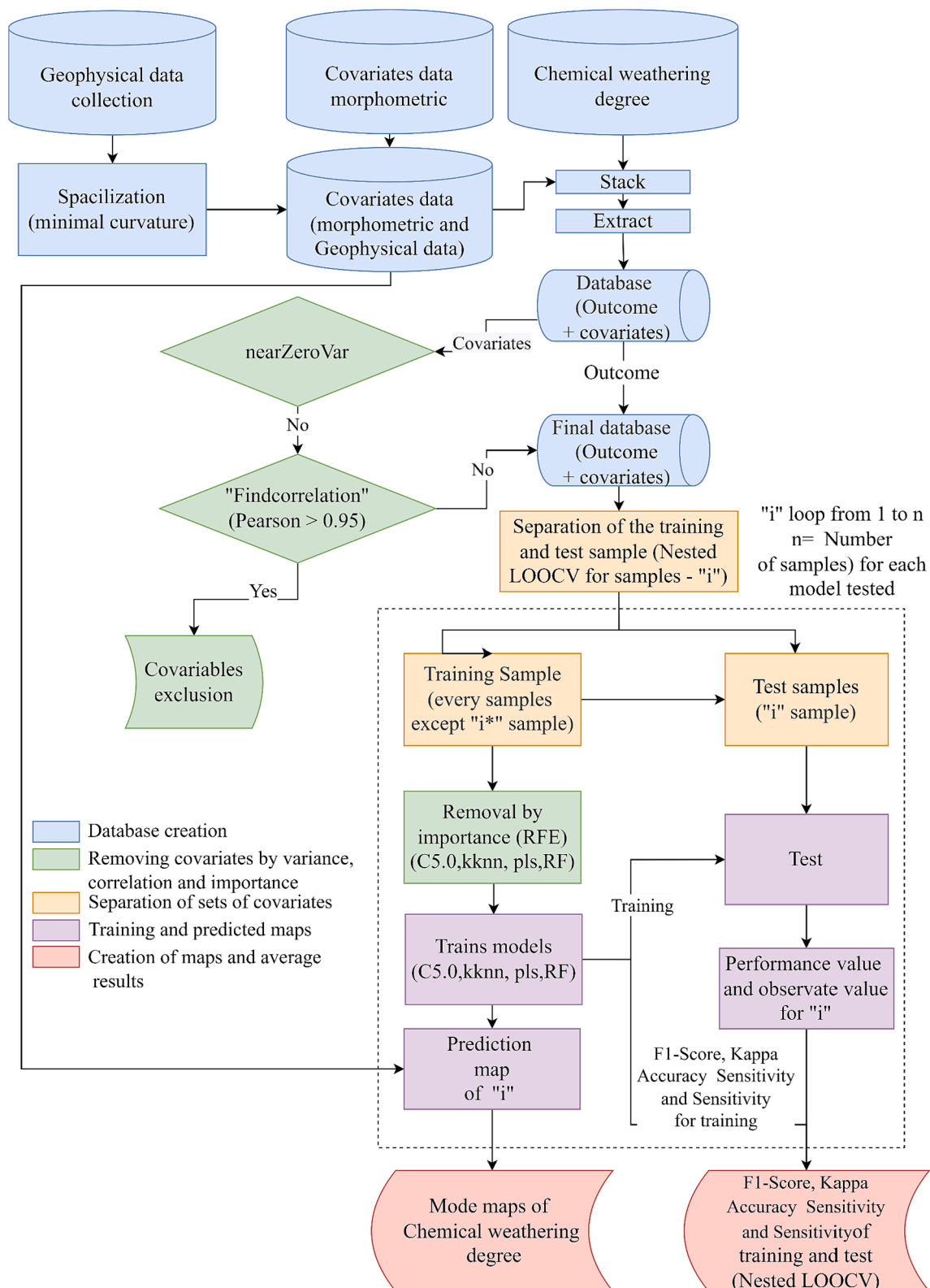
Fig. 3. Methodological flowchart showing the sequence of methodologies applied for weathering intensity prediction using geophysical and terrain attributes data.

Phase 1: The covariates that do not contribute to the modeling process were removed (those that presented a variance equal to or close to zero). The removal of non-variance covariates was performed using the "nearZeroVar" function from the *Caret* package (Kuhn et al., 2020) in the *R* software (R Core Team, 2015).

Phase 2: In this step, Sperman's correlation between pairs of

covariates was used for the removal of some variables. Pairs of variables with a high correlation (>95%) provided redundant information, and therefore, the most variable were eliminated (Darst et al., 2018). This phase was carried out using the "*find correlation*" function of the "*Caret*" package in the *R* software (Kuhn et al., 2020; R Core Team, 2015). In this step, eight covariates were eliminated: "solrad_diffuse1";

"solrad_diffuse2"; "terrain_ruggedness_index"; "solrad_ration2"; "sol-rad_direct2"; "solrad_direct1"; "valley_idx" and "curv_cross_sectional".

Phase 3: The less important covariates were removed from the models, resulting in a more parsimonious explanation of the phenomenon. In this phase we used the *Recursive Feature Elimination* (RFE) method (Kohavi and John, 1997), selecting the optimal subset of predictors based on *leave-one-out cross-validation* (LOCCV).

2.5.1. Training and testing samples and model evaluation parameters

The separation of the training and testing samples was performed using the "nested-leave-one-out-cross-validation" ("nested-LOOCV") method (Clevers et al., 2007; Honeyborne et al., 2016; Mello et al., 2022b; Rytky et al., 2020). The nested-LOOCV method is indicated for datasets with a small number of samples (in our case, the number of samples is 91, due to field limitations such as the presence of steep relief, snow banks, the presence of loose material, ridges, crevices, etc.). In such situations, the nested-LOOCV method is more suitable for performing modeling, replacing other validation/test methods (such as holdout validation) would not be viable due to the small sample set in the test and/or training group (Mello et al., 2022; Ferreira et al., 2021; Mello et al., 2022b).

The nested-LOOCV method is composed of two loops (inner and outer loops). In the inner loop, training is performed using the total dataset (n − 1), in our case, it is performed using 90 samples. In the outer loop, testing is performed; prediction is made with the sample the sample that was taken out in the inner loop. The result of this prediction is stored with the observed value of the remaining sample and later used to calculate the performance of the algorithm (Jung et al., 2020; Neogi and Dauwels, 2019). The two loops are executed once for each sample, that is, in our case they were executed 91 times, the outer loop runs 91 times and the inner loop runs 90 times, for a total of 91 × 90 runs.

All 91 samples were inserted into the outer loop, and the predicted values obtaining by the final model of each algorithm were calculated using the predicted and observed values of each sample.

The training of the models was performed after each RFE processes was performed. In the training, all selected variables for each tested algorithm from the previous step were used. In this step, leave-one-out-cross-validation (LOOCV), five values of each internal hyperparameters of each tested algorithm (*tuneLength*) were used to optimize the hyperparameters. In the final part of the training, the sample that was not predicted was used for prediction and, the result was used to evaluate the model's performance. The set of samples from the outer loop of the nested-LOOCV method was used for prediction. Five evaluation parameters were used to evaluate the model's performance: the F-1 Score test (Eq. (2), global precision of accuracy (Eq. (3), mean sensitivity (Eq. (4), mean specificity (Eq. (5) and Kappa (Eq. (6).

The F1-score is used to evaluate unbalanced data (uneven class distribution) (Sasaki, 2007). Therefore, this parameter was the main parameter used to evaluate the performance of the models, due to our unbalanced sample set. In this sense, it is used to evaluate binary classification systems, which classify examples as 'positive' or 'negative'. Therefore, this score takes false positives and false negatives into account.

$$F - 1 \ Score = \ 2*(Precision \ .Recall)/(Precision + Recall) \quad (2)$$

$$F - 1 \ Score = \ (T.P)/[(T.P) + \frac{1}{2}(F.P + F. \ N)]$$

Where:
T.P is the number of true positives.
F.P is the number of false positives.
F.N is the number of false negatives.
The accuracy indicates the overall performance of the final prediction model, that is, it indicates the probability that the studied and classified classes correspond to the true data, and it has values ranging from 0 to 1.

Table 3
Model's performance in terms of F1-Score, accuracy, kappa, sensitivity, and specificity.

Model's performance metrics	Algorithms			
	C5.0	kknn	pls	RF
F1-Score	0.55	0.43	0.48	0.49
Accuracy	0.61	0.46	0.46	0.54
Kappa	0.52	0.33	0.31	0.42
Sensitivity	0.55	0.42	0.37	0.48
Specificity	0.92	0.89	0.88	0.90

$$Accuracy = \ \frac{\sum^{x}i}{n} \ x \ 100 \quad (3)$$

Where:
xi = sum of all diagonal elements of the confusion matrix.
n = total number of samples.
The sensitivity represents the ability of models to predict the correct values of a class, while the specificity represents the ability of a model to correctly predict that samples are not contained in a given class.

$$Sensibility = \ \frac{\sum_1^n \left(\frac{TP}{TP \ + \ FN} \right)}{n} \quad (4)$$

$$Specificity = \frac{\sum_1^n \left(\frac{TN}{TN \ + \ FP} \right)}{n} \quad (5)$$

Where:
TP = number of true positives.
FP = false positives.
TP = false negatives.
n = number of existing classes.
Kappa (K) indices depict the degree of agreement between the prediction of results and reference values. Kappa indices are used as the basis of the confusion matrix (Ben-David, 2008) (Eq. (4)). The value of K ranges from 0 (no agreement) to 1 (almost perfect) (Landis and Koch, 1977).

$$K = \frac{p_0 - p_e}{1 - p_e} \quad (6)$$

Where:
K = Kappa estimate.
p_o = is the relative observed agreement among raters.
pe = is the hypothetical probability of chance agreement.

2.5.2. Generation of final CWI maps

Selection using the RFE method was repeated 91 times with different training and testing samples. The generated results were analyzed, and the performance metrics of the models (F1-Score test, Kappa, Accuracy, Sensitivity and Sensitivity) were evaluated. The prediction error of each algorithm was also analyzed by evaluating the coefficient of variation. Then, the final map was created by combining the 91 prediction maps generated for each algorithm tested. A final weathering intensity map (CWI) was created with the modal value of each pixel.

The CWI final map was chosen based on the best F1-Score and Kappa performance and, the previous model's parameters were used to extract the geophysical data and weathering intensity values at the sampling points.

3. Results and discussion

3.1. Model performance, uncertainty and covariate's importance

The C5.0 algorithm showed the best performance in modeling the CWI, followed by RF (Table 3). Based on 91 runs, C5.0 had the highest F-1 score (0.55), Kappa (0.52), accuracy (0.61), sensitivity (0.55), and
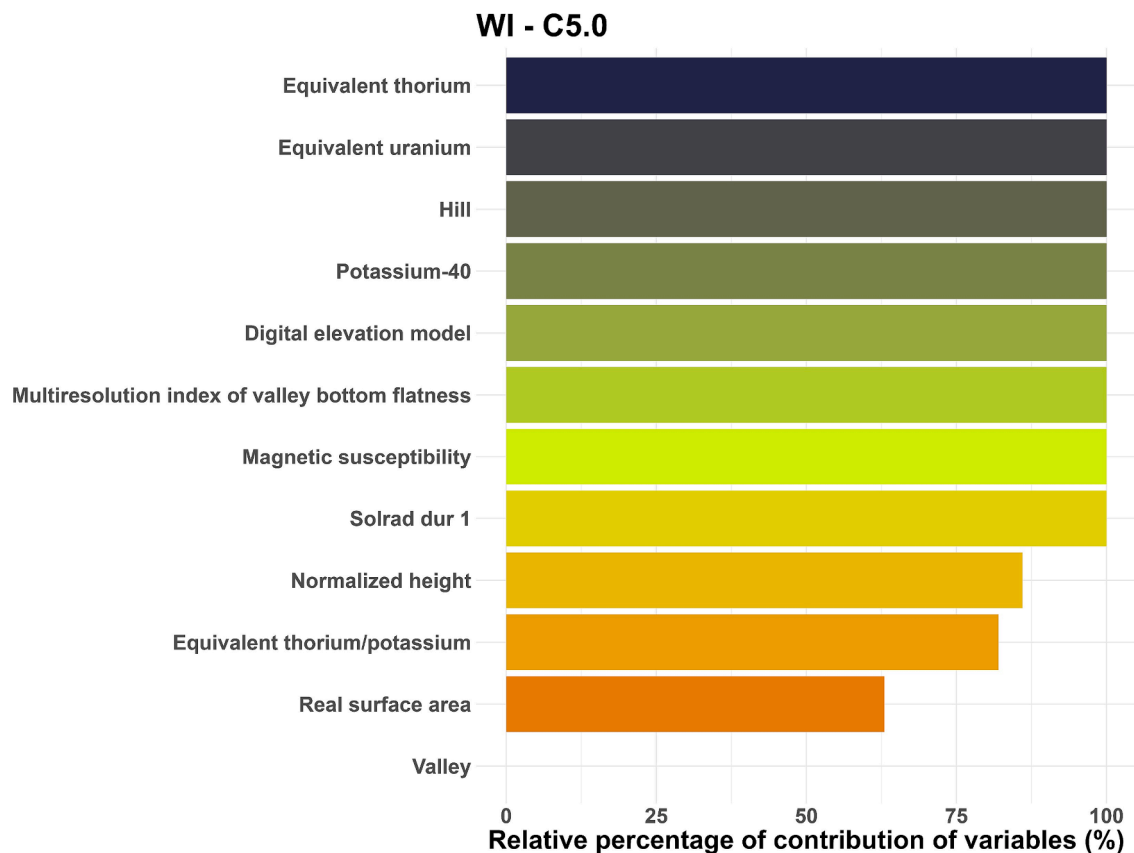
WI - C5.0

Fig. 4. Importance of variables of predictors. *X* axis: variables that most contributed to the predictive models. Axis *y*: value in relative percentage of the contribution.

sensibility (0.92) values (Table 3). Therefore, the C5.0 algorithms were selected for the spatial prediction of the weathering intensity.

The C5.0 algorithm modeled the CWI using topographic and geophysical data, in addition to ranking the degree of weathering of rocks as an outcome variable ("*y*") in the modeling. Our results are consistent with those obtained by Su et al., (2021) and Tanyu et al., (2021), who used C5.0 to estimate the soil landslide susceptibility and achieved a better performance compared to RF. Although the C5.0 algorithm presented a better performance, the F1-Score was not higher than 0.55 (Table 3). Probably, this F1-Score value may be related to: *i)* the high heterogeneity of the lithology in the area (six lithological classes within 500 ha); *ii)* the limited distribution of samples in some lithological substrates (unbalanced data due to the presence of permanent snowbanks or challenging to access steep terrain); and *iii)* the slight variation in the dataset (Mello et al., 2020; Mello et al., 2021). In addition, an *in-situ* evaluation using geophysical sensors has several uncontrolled factors, such as the presence of rock fragments and different degrees of moisture that are a function of a highly dynamic and unstable local climate and are associated with melting water, and the deposition of sediments through solifluction/erosion over the original lithology (Reinhardt and Herrmann, 2019). These factors make the area complex (Parshin et al., 2018) and, may negatively impact the prediction of the weathering index. However, the samples were collected in the most accessible parts of the area, and at the same time, the lithological representativeness of the area was ensured.

The nested-LOOCV method used to separate the training and testing samples was appropriate for our dataset, as it contains 91 samples due to the field complexity and limitations (Clevers et al., 2007; Ferreira et al., 2021; Honeyborne et al., 2016; Rytky et al., 2020). In this case, our dataset could provide an unbiased estimate of the true error if another method was used (Chen et al., 2017; Li et al., 2018; Xing et al., 2011; Xu et al., 2020).

The importance of covariates in predicting the CWI showed that eTh, ^{40}K, ^{40}K/eTh, ^{40}K/eU, κ, the DEM, the multiresolution index of valley bottom flatness (MRVBF), the insolation duration for the month of January (Solrad Diffuse1), and normalized height (NH) were the most important variables for predicting the weathering intensity using the C5.0 model, contributing 75–100% to the mean accuracy (Fig. 4).

The eTh, ^{40}K and κ contents, as well as the eTh/^{40}K and eU/^{40}K ratios are closely related to the lithology (Fig. 4), and the results reinforce the association with the CWI (Ayoubi et al., 2018; De Jong et al., 2000; Mello et al., 2022; Dickson and Scott, 1997; Jordanova, 2016; Mullins, 1977; Wilford, 2012; Wilford and Minty, 2006; Wilford and Thomas, 2012; Wilford et al., 1997).

The MRVBF (Fig. 4), indicates the presence of flat surfaces at the bottom of a valley and places where liquid water from melting ice or precipitation can remain for long periods of time, accelerating chemical weathering. The Solrad Diffuse1 variable corresponds to the highest intensity of solar radiation in Antarctica. This factor, associated with the dark rocks, the higher rate of liquid precipitation at that time and the wide range of thermal variations cryoclast the rocks (Grotzinger and Jordan, 2013; Teixeira et al., 2009), and this is intensified by certain rock features, such as the porosity and fissures that contribute to increases in cryoclastic processes (Walder and Hallet, 1985). Concomitantly, this increases the degree of chemical weathering. In addition, Solrad Diffuse1 affects the intensity of the evaporation of water from the lithologic substrate due to differences in substrate temperature regimes. As a result, it affects the weathering intensity as well (Boland et al., 2008), by changing both the water residence time and activity (Mattigod and Kittrick, 1980).

The NH correspond to the vertical distance between the base and ridge of a normalized slope (Fig. 4). The NH associated with the DEM demonstrated the effect of altitude on the weathering intensity, the coldest part is located at high altitudes and warmest part is at the lowest
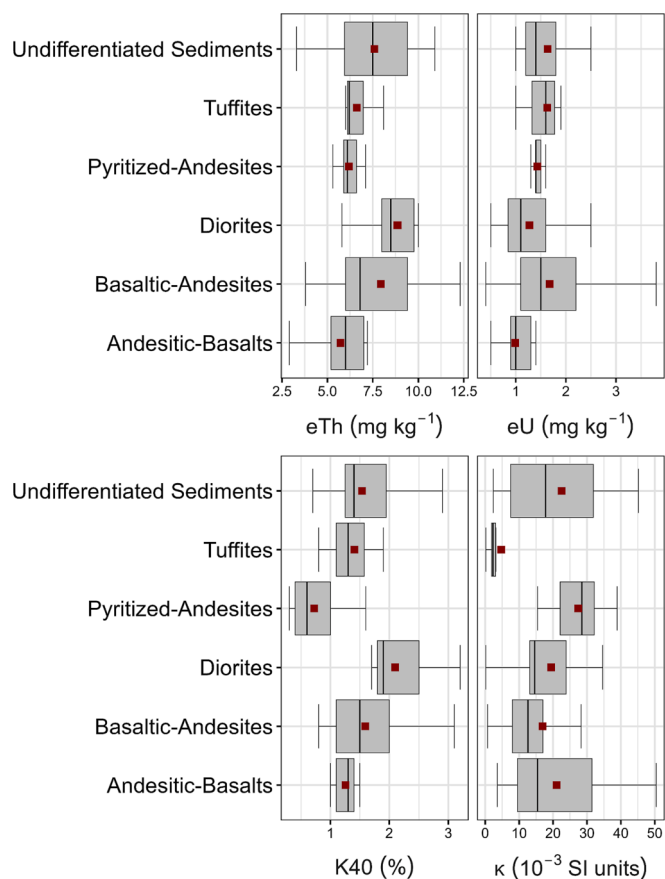
Fig. 5. Boxplot with descriptive statistics of the distribution of radionuclide contents and magnetic susceptibility by lithology.

altitude. In addition, the erodibility increases for steep terrain, reducing the chemical weathering intensity, despite that the fact that the density of cracks tends to increase with height (Shobe et al., 2017). Thus, due to these morphometric variables, chemical weathering tends to be reduced in the upper parts of the peninsula with steep terrain.

3.2. Chemical weathering intensity and geophysical variables

The highest levels of eTh and ^{40}K occurred on diorites, while the greater eU level occurred on basaltic-andesites (Fig. 5). The mean κ values were low in all lithologies, notably in tuffites, followed by andesitic-basalts (Fig. 5). The highest mean κ values were observed on the pyritized-andesites, which are mesocratic rocks, but have high levels of sulfides (pyrite) (Fig. 5).
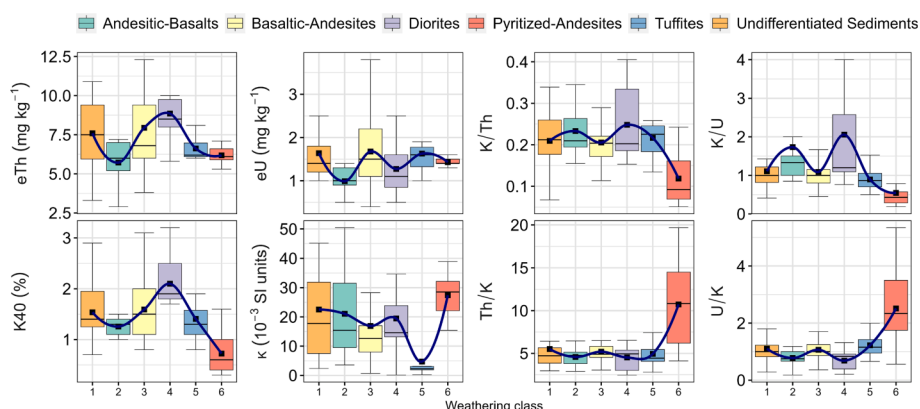
The contents of the radionuclides eTh and ^{40}K (Fig. 5) are in agreement with the results of Guagliardi et al., (2013), Dickson & Scott, (1997), Wilford et al. (1997) and Arnedo et al. (2017). These authors found higher levels of radionuclides in felsic igneous rocks (richer in Si) and lower levels in mafic igneous rocks (richer in Fe). The variation of the eU content in different igneous rocks, as in our case, has already been studied by several researchers (Cunningham et al., 1982; Henderson et al., 1971; Larsen and Gottfried, 1960; Rogers and Ragland, 1961), and the most plausible explanation for this is the loss of uranium via oxidation during the later stages of igneous differentiation (Rogers and Ragland, 1961), which results in a large variability. Another factor that may be causing the greater variability of eU is the different stages of oxidation of this element, which vary depending on the environment (Dickson and Scott, 1997).

The mean κ values (Fig. 5) were low, even in mafic lithologies such as basaltic-andesites /andesitic-basalts, where greater values were expected. Mullins (1977) demonstrated a relationship between an increase in the ferrimagnetic mineral content in the parent material and an increase in the κ value. However, in the present case, as many of the rocks are covered by shallow drift deposits, or are affected by mixing, this may have interfered with the κ values; the neoformation of ferrimagnetic minerals in soils in periglacial environments may have be reduced due to the lower rate of iron release caused by chemical weathering and lower temperatures (Schwertmann, 1988). On the other hand, greater κ values on pyritized-andesites, result from sulfidation (Passier et al., 2001), which causes the formation of pyrite in the pyritized-andesites, along pyrrhotite and magnetite, and enhanced chemical weathering (Figueiredo, 2000), concentrating the ferrimagnetic minerals, and contributing to the greater κ values.

Fig. 6 shows the descriptive statistics using box-plots for each of the geophysical variables and weathering classes by lithology. There are trends in the behavior of the eU, eTh and ^{40}K radionuclides as the weathering progresses from class 1 to class 6. There was a reduction in the ^{40}K content, which shows a greater mobility and depletion during chemical weathering.

The eTh and eU radionuclides showed variations; eTh had a tendency to increase from class 1 to 4 and, then decrease (Fig. 6). eU presented the greater variability across weathering classes, with a decreasing trend for class 6. Thus, the κ values, decreased as the increasing chemical weathering intensity increased (Fig. 6).

In general, the intensity at which chemical weathering operates in the periglacial environment in M.A. is lower compared to a tropical environment. Thus, the ^{40}K contents were relatively high for all lithologies, except in sulfated areas (pyritized-andesites – class 6) where active hydrolysis and leaching acted with greater intensity, reducing the ^{40}K contents. According to Dickson and Scott, (1997) and Wilford and Thomas, (2012), this radionuclide is highly mobile and tends to be removed from the system if the intensity of chemical weathering is high in a free draining environment. Regarding the eTh and eU contents, they
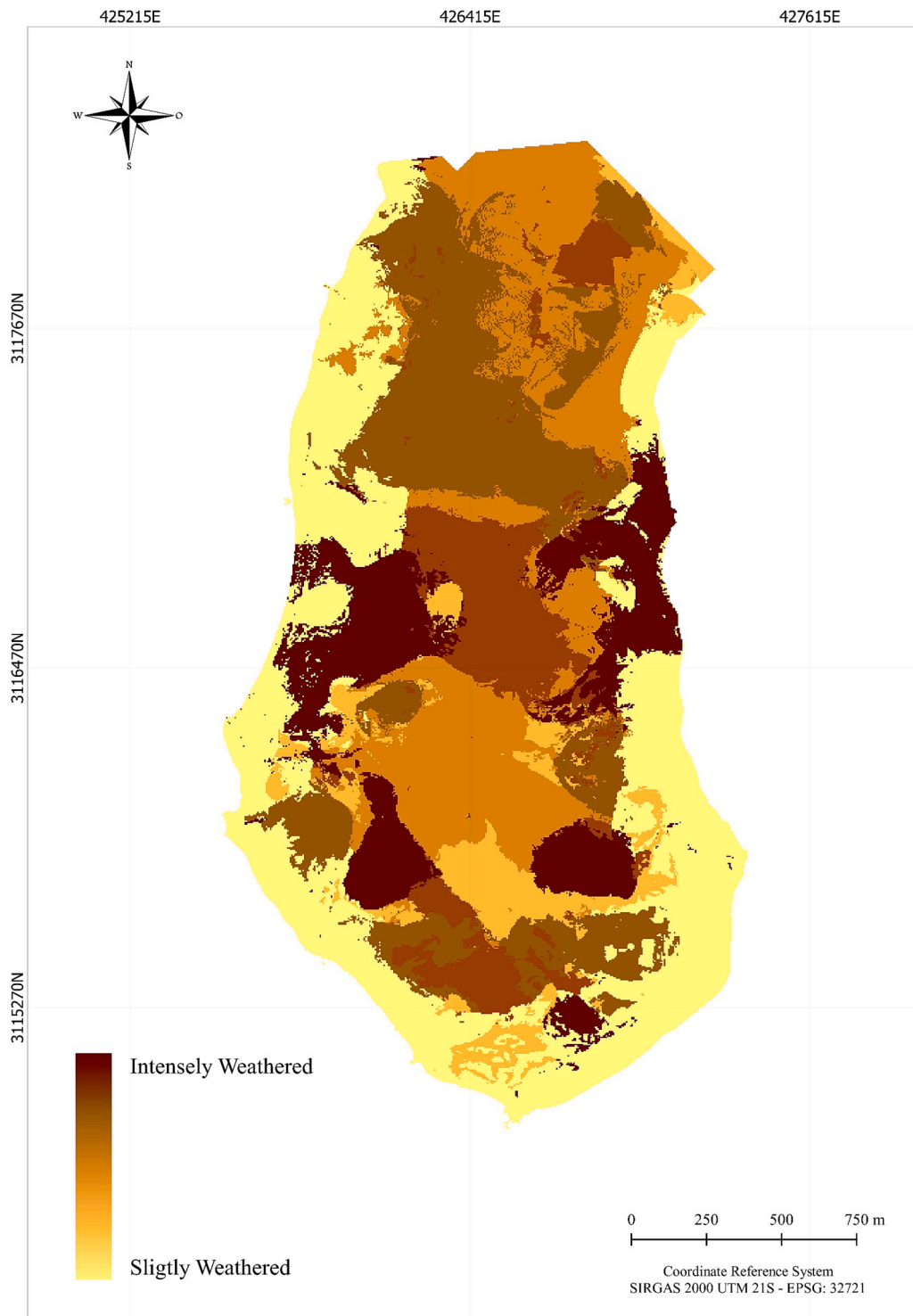

Fig. 6. Box-plots for each of the environmental variables with descriptive statistics of the distribution of radionuclide contents and magnetic susceptibility, radionuclides rates related to chemical weathering by lithology. The middle line identifies the medium sample value and the connected line intersects the mean value. The numbers on the x-axis (1 to 6) indicate the weathering class. In other words, this is the boxplots for each of the environmental variables with descriptive statistics of the distributions of radionuclide contents and the magnetic susceptibility, where the radionuclide rates are related to the chemical weathering intensity by lithology.

Fig. 7. Weathering intensity index. Class 1 corresponds to the least weathered rock and class 6 corresponds to the most chemically weathered rock.

ranged from low to moderate for all lithologies, evidencing the relatively low rate at which chemical weathering occurs in the area. These radionuclides tend to accumulate residually and increase when as chemical weathering operates with a greater intensity, as evidenced in weathering class 6 for over pyritized-andesites (Dickson and Scott, 1997; Wilford, 2012; Wilford et al., 1997).

The ratios ^{40}K/eTh and ^{40}K/eU decreased from the class 1 to class 6, indicating an increase in the chemical weathering intensity according to the lithology. Conversely, the inverse ratios of these eTh/^{40}K and eU/^{40}K radionuclides increased from class 1 to class 6, corroborating the

increase in the intensity of chemical weathering (Fig. 6). Both behaviors are related to the loss of ^{40}K and the residual accumulation of eTh and eU, as the rates of chemical weathering increase, as previously discussed.

The behavior of the κ values in the periglacial environment is the opposite of the κ value behavior those observed in a tropical environment on similar lithologies (Mello et al., 2022; Mello et al., 2020). In periglacial environments, the conditions for the neoformation of ferrimagnetic minerals are constrained by the low temperature and low iron release rate (Schwertmann, 1988; Grimley and Vepraskas, 2000;
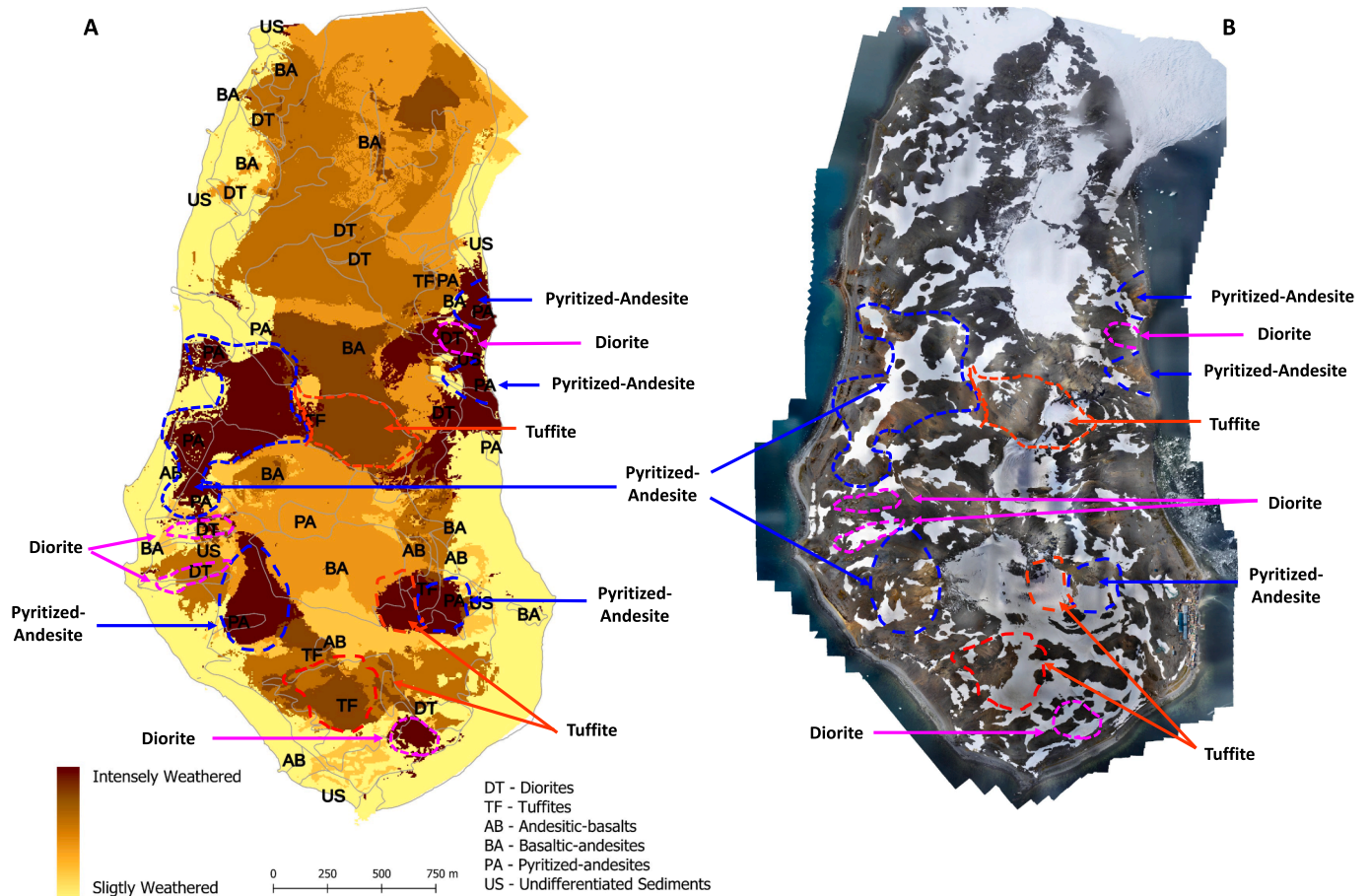
Fig. 8. A) Predicted map of chemical weathering intensity vs lithology type; B). Areas where chemical weathering operates at higher intensities.

Maxbauer et al., 2016). However, for the pyritized-andesites (class 6) the oxidation of pyrite releases higher levels of iron that can be used for the neoformation of ferrimagnetic minerals, increasing κ values.

3.3. Weathering intensity and its relationship with lithology

The predicted intensity at which chemical weathering operates in the study area is shown in Fig. 7. In general, we observed that the most weathered areas are located on the pyritized-andesites lithologies, followed by the tuffites (Fig. 8a and b). Subsequently, intermediate weathered areas occur on diorites. The basaltic-andesites and andesitic-basalts have similar chemical weathering degrees. The least chemically weathered areas are the coastal marine undifferentiated sediments (Fig. 8a).

The presence of pyrite in the pyritized-andesites generates natural acid drainage on this lithology and parts of the surrounding rocks. In this naturally acidic environment (via sulfurization), there is a drastic reduction in the pH of the environment. As a result, hydrolysis is highly pronounced on/near lithological substrates and soils in M.A. (de Souza et al., 2012; Dold et al., 2013; Simas et al., 2006). At these points, the highest rates of chemical weathering on Keller Peninsula occur (Fig. 8a and b), and the rocks are covered with a sulfurized crust of oxidized pyrite that is easily observed in the field (**supplementary material, image 2**). Thus, even though the pyritized-andesites have a greater resistance to weathering than tuffite, they are more weathered due to the sulfurization that occurs in the area.

The second highest rate at which chemical weathering operates is found on tuffite areas (Fig. 8a and b). These rocks have the greatest susceptibility to chemical weathering due to the mineralogical composition (less resistant minerals) and structural characteristics of the rock (high porosity) (Fabris et al., 1994). However, due to the absence of pyrite, these rocks show the second-lowest degree of resistance to weathering.

The areas in which chemical weathering operates with intermediate intensities are found on diorites (Fig. 8a). This rock occurs in smaller proportions in the study area and its mineralogical composition is similar to that of andesite (Grotzinger and Jordan, 2013; Teixeira et al., 2009). However, the granulometry of diorite is larger, meaning that it has the third-lowest degree of resistance to weathering; this substrate has the third-most chemically weathered lithology.

The intensities at which chemical weathering operates on andesitic-basalts and basaltic-andesites are similar (Fig. 8a). This is probably due to the mineralogical and structural characteristics of these rocks, which both transition from mafic to intermediate and from intermediate to mafic in color and, consequently in mineralogical composition (Grotzinger and Jordan, 2013; Teixeira et al., 2009). Generally, the basaltic-andesites have greater feldspar contents and larger crystals, while the andesitic-basalts have a higher pyroxene content and a smaller crystal size. Thus, the larger size of the andesite crystals has a similar effect to the less resistant basalt minerals, resulting in similar intensities of chemical weathering in these two groups of rocks.

The areas on the undifferentiated marine sediments tend to correspond to the least chemically weathered areas, and they contain the most physically reworked material. (Fig. 8a). The explanation for this is

probably associated with the greater diversity of rocks in this environment, which are mainly granitic, with low chemical alteration.

4. Conclusions

Chemical weathering in M. A. is not very intense, but in some areas with peculiar characteristics, such as sulfide-affected areas (over pyritized-andesites), show a higher chemical weathering intensity, due to enhanced hydrolysis caused by sulfurization after pyrite decomposition. This was clearly detected by the geophysical data and in the field characteristics observed in the rocks.

The C5.0 algorithm performed better than RF in predicting the weathering intensity for this periglacial environment, presenting the highest model performance metrics. It obtained the highest F1-score, accuracy, Kappa, sensitivity and specificity values. The most important variables in predicting the weathering intensity were eTh, ^{40}K, ^{40}K/eTh, ^{40}K/eU, κ, the DEM, the MRVBF, the insolation duration for the month of January (Solrad Diffuse1) and the NH. In fact, these variables control and/or are modified by the degree of chemical weathering.

The radionuclide contents and magnetic susceptibility in the rocks were variable, but there was a tendency to follow values previously reported in the literature. Regarding the ^{40}K/eTh, ^{40}K/eU, eTh/^{40}K and eU/^{40}K ratios, the behavior followed the patterns reported in the literature; these values are good indicators of the intensity of chemical weathering.

The contents of radionuclides and ferrimagnetic minerals present in different lithologies, depend on the intensity of chemical weathering operates. On the other hand, the stability and distribution of these elements in this cold environment are influenced by periglacial processes that occurs throughout the landscape (cryoturbation, solifluction, cryoclastic processes, the advance and retreat of glaciers and, cryoplanation, among others).

The chemical degree of alteration of the rocks was efficiently modeled as the "y" variable based on the mineralogical composition, texture and structure of the rocks, which were, associated with field observations of features and the intensity of chemical weathering. The chemical weathering intensity prediction model using gamma spectrometric and magnetic data closely matched the in-situ evaluation of the chemical degree of alteration. The pyritized-andesites showed the highest intensities of weathering, followed by tuffites, diorites, andesitic-basalts, basaltic-andesites, and finally undifferentiated marine sediments.

The contents of radionuclides and their ratios, κ, landform attributes and lithological characteristics (related to the chemical weathering resistance/degree) were successfully used to model the chemical weathering intensity in the periglacial environment of M.A. Periglacial processes contributed to the distribution and stability of the radionuclide contents and κ.

Declaration of Competing Interest

The authors declare that they have no known competing financial interests or personal relationships that could have appeared to influence the work reported in this paper.

Data availability

Data will be made available on request.

Appendix A. Supplementary data

Supplementary data to this article can be found online at https://doi.org/10.1016/j.geoderma.2023.116615.

References

Arnedo, M.A., Rubiano, J.G., Alonso, H., Tejera, A., González, A., González, J., Gil, J.M., Rodríguez, R., Martel, P., Bolivar, J.P., 2017. Mapping natural radioactivity of soils in the eastern Canary Islands. J. Environ. Radioact. 166, 242–258. https://doi.org/10.1016/j.jenvrad.2016.07.010.

Ayoubi, S., Abazari, P., Zeraatpisheh, M., 2018. Soil great groups discrimination using magnetic susceptibility technique in a semi-arid region, central Iran. Arab. J. Geosci. 11 https://doi.org/10.1007/s12517-018-3941-4.

Beamish, D., 2013. Gamma ray attenuation in the soils of Northern Ireland, with special reference to peat. J. Environ. Radioact. 115, 13–27. https://doi.org/10.1016/j.jenvrad.2012.05.031.

Beamish, D., 2015. Relationships between gamma-ray attenuation and soils in SW England. Geoderma 259–260, 174–186. https://doi.org/10.1016/j.geoderma.2015.05.018.

Ben-David, A., 2008. About the relationship between ROC curves and Cohen's kappa. Eng. Appl. Artif. Intell. 21 (6), 874–882.

Birkenmajer, K., 1980. Geology of Admiralty Bay, King George Island (South Shetland Islands)—an outline. Polish Polar Res. 1, 29–54.

Blundell, A., Dearing, J.A., Boyle, J.F., Hannam, J.A., 2009. Controlling factors for the spatial variability of soil magnetic susceptibility across England and Wales. Earth-Sci. Rev. 95, 158–188. https://doi.org/10.1016/j.earscirev.2009.05.001.

Boland, J., Ridley, B., Brown, B., 2008. Models of diffuse solar radiation. Renew. Energy 33 (4), 575–584.

Brenning, A., 2008. Statistical geocomputing combining R and SAGA: The example of landslide susceptibility analysis with generalized additive models. Hamburg. Beiträge zur Phys. Geogr. und Landschaftsökologie 19, 410.

Buss, H.L., Chapela Lara, M., Moore, O.W., Kurtz, A.C., Schulz, M.S., White, A.F., 2017. Lithological influences on contemporary and long-term regolith weathering at the Luquillo Critical Zone Observatory. Geochim. Cosmochim. Acta 196, 224–251. https://doi.org/10.1016/j.gca.2016.09.038.

Cabral Pinto, M.M.S., Silva, M.M.V.G., Ferreira da Silva, E.A., Dinis, P.A., Rocha, F., 2017. Transfer processes of potentially toxic elements (PTE) from rocks to soils and the origin of PTE in soils: A case study on the island of Santiago (Cape Verde). J. Geochem. Explor. 183, 140–151. https://doi.org/10.1016/j.gexplo.2017.06.004.

Carroll, D., 2012. Rock Weathering. Springer Science & Business Media.

Chen, X., Zhang, H., Lee, S.-W., Shen, D., 2017. Hierarchical high-order functional connectivity networks and selective feature fusion for MCI classification. Neuroinformatics 15 (3), 271–284.

Chesworth, W., 2008. Encyclopedia of soil science.

Chittleborough, D.J., 1991. Indices of weathering for soils and palaeosols formed on silicate rocks. Aust. J. Earth Sci. 38 (1), 115–120.

Clevers, J.G.P.W., Van Der Heijden, G.W.A.M., Verzakov, S., Schaepman, M.E., 2007. Estimating grassland biomass using SVM band shaving of hyperspectral data. Photogramm. Eng. Remote Sens. 73, 1141–1148. https://doi.org/10.14358/PERS.73.10.1141.

Cristina Barbosa Guimarães, C., A. M. Demattê, J., Carlos de Azevedo, A., Simão Diniz Dalmolin, R., ten Caten, A., Sayão, V.M., Cipriano da Silva, R., Poppiel, R.R., Mendes, W.d.S., Urbina Salazar, D.F., Barros e Souza, A., 2021. Soil weathering behavior assessed by combined spectral ranges: Insights into aggregate analysis. Geoderma 402, 115154.

Cunningham, C.G., Ludwig, K.R., Naeser, C.W., Weiland, E.K., Mehnert, H.H., Steven, T. A., Rasmussen, J.D., 1982. Geochronology of hydrothermal uranium deposits and associated igneous rocks in the eastern source area of the Mount Belknap Volcanics, Marysvale. Utah. Econ. Geol. 77, 453–463.

Darst, B.F., Malecki, K.C., Engelman, C.D., 2018. Using recursive feature elimination in random forest to account for correlated variables in high dimensional data. BMC Genet. 19, 65.

De Jong, E., Pennock, D.J., Nestor, P.A., 2000. Magnetic susceptibility of soils in different slope positions in Saskatchewan, Canada. Catena 40, 291–305. https://doi.org/10.1016/S0341-8162(00)00080-1.

Mello, D.C. de, Ferreira, T.O., Veloso, G.V., Lana, M.G. de, Mello, F.A. de O., Di Raimo, L. A.D.L., Cabrero, D.R.O., Souza, J.J.L.L. de, Fernandes-Filho, E.I., Francelino, M.R., 2022a. Weathering intensities in tropical soils evaluated by machine learning, clusterization and geophysical sensors. SOIL Discuss. 1–41.

de Souza, J.J.L.L., Schaefer, C.E.G.R., Abrahão, W.A.P., de Mello, J.W.V., Simas, F.N.B., da Silva, J., Francelino, M.R., 2012. Hydrogeochemistry of sulfate-affected landscapes in Keller Peninsula, Maritime Antarctica. Geomorphology 155, 55–61.

Dickson, B.L., Scott, K.M., 1997. Interpretation of aerial gamma-ray surveys – adding the geochemical factors. AGSO J. Aust. Geol. Geophys. 17, 187–200.

Doetterl, S., Berhe, A.A., Arnold, C., Bodé, S., Fiener, P., Finke, P., Fuchslueger, L., Griepentrog, M., Nordt, L.C., Harden, J.W., Nadeu, E., Schnecker, J., Six, J., Trumbore, S., Van Oost, K., Vogel, C., Boeckx, P., 2018. Links among warming, carbon and microbial dynamics mediated by soil mineral weathering. Nat. Geosci. 11, 589–593. https://doi.org/10.1038/s41561-018-0168-7.

Dold, B., Gonzalez-Toril, E., Aguilera, A., Lopez-Pamo, E., Cisternas, M.E., Bucchi, F., Amils, R., 2013. Acid rock drainage and rock weathering in Antarctica: important sources for iron cycling in the Southern Ocean. Environ. Sci. Technol. 47 (12), 6129–6136.

Driese, S.G., Nordt, L.C., Stinchcomb, G.E., 2021. Soils, chemical weathering, and climate change in Earth history. Hydrogeol. Chem. Weather. soil Form. 21–65.

Duval, J.S., 1990. Modern aerial gamma-ray spectrometry and regional potassium map of the conterminous United States. J. Geochem. Explor. 39, 249–253. https://doi.org/10.1016/0375-6742(90)90076-M.

Dynarski, K.A., Morford, S.L., Mitchell, S.A., Houlton, B.Z., 2019. Bedrock nitrogen weathering stimulates biological nitrogen fixation. Ecology 100, 1–10. https://doi.org/10.1002/ecy.2741.

Fabris, J.D., Coey, J.M.D., de Jesus Filho, M.F., Santana, D.P., Goulart, A.T., Fontes, M.F., Curi, N., 1994. Mineralogical analysis of a weathering mantle derived from tuffite. Hyperfine Interact. 91 (1), 751–757.

Ferreira, R.G., Silva, D.D.d., Elesbon, A.A.A., Fernandes-Filho, E.I., Veloso, G.V., Fraga, M.d.S., Ferreira, L.B., 2021. Machine learning models for streamflow regionalization in a tropical watershed. J. Environ. Manage. 280, 111713.

Figueiredo, B.R., 2000. Minérios e ambiente. Editora da UNICAMP.

Francelino, M.R., Schaefer, C.E.G.R., Simas, F.N.B., Filho, E.I.F., de Souza, J.J.L.L., da Costa, L.M., 2011. Geomorphology and soils distribution under paraglacial conditions in an ice-free area of Admiralty Bay, King George Island, Antarctica. Catena 85 (3), 194–204.

Franke, W.A., 2009. The durability of rocks—developing a test of rock resistance to chemical weathering. Am. J. Sci. 309 (8), 711–730.

Gomes, L.C., Faria, R.M., Souza, E.D., Veloso, G.V., Ernesto, C., Schaefer, G.R., Inácio, E., Filho, F., 2019. Modelling and mapping soil organic carbon stocks in Brazil. Geoderma 340, 337–350. https://doi.org/10.1016/j.geoderma.2019.01.007.

Grasty, R.L., Holman, P.B., Blanchard, Y.B., 1991. Transportable calibration pads for ground and airborne gamma-ray spectrometers. Geological Survey of Canada.

Grimley, D.A., Vepraskas, M.J., 2000. Magnetic susceptibility for use in delineating hydric soils. Soil Sci. Soc. Am. J. 64, 2174–2180. https://doi.org/10.2136/sssaj2000.6462174x.

Grotzinger, J., Jordan, T., 2013. Para Entender a Terra-6. Bookman Editora.

Guagliardi, I., Buttafuoco, G., Apollaro, C., Bloise, A., De Rosa, R., Cicchella, D., 2013. Using gamma-ray spectrometry and Geostatistics for assessing geochemical behaviour of radioactive elements in the lese catchment (southern Italy). Int. J. Environ. Res. 7, 645–658. https://doi.org/10.22059/ijer.2013.644.

Hall, K., Thorn, C., Sumner, P., 2012. On the persistence of 'weathering'. Geomorphology 149, 1–10.

Hasri, N.N.M., Wen, N.H., Howe, C.W., Mohamad, M.S., Deris, S., Kasim, S., 2017. Improved support vector machine using multiple SVM-RFE for cancer classification. Int. J. Adv. Sci. Eng. Inf. Technol. 7, 1589–1594.

Henderson, P., Mackinnon, A., Gale, N.H., 1971. The distribution of uranium in some basic igneous cumulates and its petrological significance. Geochim. Cosmochim. Acta 35, 917–925. https://doi.org/10.1016/0016-7037(71)90005-6.

Hijmans, R.J., Van Etten, J., 2016. raster: Geographic Data Analysis and Modeling. R package version 2.5-8.

Honeyborne, I., McHugh, T.D., Kuittinen, I., Cichonska, A., Evangelopoulos, D., Ronacher, K., van Helden, P.D., Gillespie, S.H., Fernandez-Reyes, D., Walzl, G., Rousu, J., Butcher, P.D., Waddell, S.J., 2016. Profiling persistent tubercle bacilli from patient sputa during therapy predicts early drug efficacy. BMC Med. 14, 1–13. https://doi.org/10.1186/s12916-016-0609-3.

INPE, 2009. Instituto Nacional de Pesquisas Espaciais [WWW Document].

Jackson, M.L., Sherman, G.D., 1953. Chemical weathering of minerals in soils. Adv. Agron. 5, 219–318. https://doi.org/10.1016/S0065-2113(08)60231-X.

Jenny, H., 1994. Factors of Soil Formation: A System of Quantitative Pedology. Dover Publication, New York.

Jordanova, N., 2016. Soil Magnetism: Applications in Pedology. Academic Press, Environmental Science and Agriculture.

Jung, Y., Lee, J., Lee, M., Kang, N., Lee, I., 2020. Probabilistic analytical target cascading using kernel density estimation for accurate uncertainty propagation. Struct. Multidiscip. Optim. 61 (5), 2077–2095.

Khelfaoui, M., Medjram, M.S., Kabir, A., Zouied, D., Mehri, K., Chikha, O., Trabelsi, M.A., 2020. Chemical and mineralogical characterization of weathering products in mine wastes, soil, and sediment from the abandoned Pb/Zn mine in Skikda, Algeria. Environ. Earth Sci. 79, 1–15. https://doi.org/10.1007/s12665-020-09043-x.

Kohavi, R., John, G.H., 1997. Wrappers for feature subset selection. Artif. Intell. 97 (1-2), 273–324.

Kuhn, M., Wing, J., Weston, S., Williams, A., Keefer, C., Engelhardt, A., Cooper, T., Mayer, Z., Kenkel, B., Team, R.C., 2020. Package 'caret.' R J.

Landis, J.R., Koch, G.G., 1977. The measurement of observer agreement for categorical data. Biometrics 33 (1), 159.

Larsen, E.S., Gottfried, D., 1960. Uranium and thorium in selected suites of igneous rocks. Am. J. Sci. 258.

Li, Y., Liu, J., Huang, J., Li, Z., Liang, P., 2018. Learning brain connectivity sub-networks by group-constrained sparse inverse covariance estimation for Alzheimer's disease classification. Front. Neuroinform. 12, 58.

Lopes, D.d.V., Schaefer, C.E.G.R., Souza, J.J.L.L.d., Oliveira, F.S.d., Simas, F.N.B., Daher, M., Gjorup, D.F., 2019. Concretionary horizons, unusual pedogenetic processes and features of sulfate affected soils from Antarctica. Geoderma 347, 13–24.

Lopes, D., Vale, D.O., Oliveira, F.S., Souza, J.J.L.L.D.E., Machado, M.D.E.R., Schaefer, C.E.G.R., 2022a. Soil pockets phosphatization and chemical weathering of sites affected by flying birds of Maritime Antarctica. An. Acad. Bras. Cienc. 94.

Lopes, D., Soares de Oliveira, F., Pereira, T.T.C., Schaefer, C.E.G.R., 2022b. Pedogeomorphology and weathering at Snow Island, Maritime Antarctica. Catena 217, 106515.

Mattigod, S.V., Kittrick, J.A., 1980. Temperature and water activity as variables in soil mineral activity diagrams. Soil Sci. Soc. Am. J. 44 (1), 149–154.

Maxbauer, D.P., Feinberg, J.M., Fox, D.L., 2016. Magnetic mineral assemblages in soils and paleosols as the basis for paleoprecipitation proxies: A review of magnetic methods and challenges. Earth-Sci. Rev. 155, 28–48. https://doi.org/10.1016/j.earscirev.2016.01.014.

McCafferty, A.E., Van Gosen, B.S., 2009. Airborne gamma-ray and magnetic anomaly signatures of serpentinite in relation to soil geochemistry, northern California. Appl. Geochemistry 24, 1524–1537. https://doi.org/10.1016/j.apgeochem.2009.04.007.

McFadden, M., Scott, W.R., 2013. Broadband soil susceptibility measurements for EMI applications. J. Appl. Geophys. 90, 119–125. https://doi.org/10.1016/j.jappgeo.2013.01.009.

Mello, D., Alexandre Melo Demattê, J., Alcantara de Oliveira Mello, F., Roberto Poppiel, R., ElizabetQuiñonez Silvero, N., Lucas Safanelli, J., Barros e Souza, A., Augusto Di Loreto Di Raimo, L., Rizzo, R., Eduarda Bispo Resende, M., Ernesto Gonçalves Reynaud Schaefer, C., 2021. Applied gamma-ray spectrometry for evaluating tropical soil processes and attributes. Geoderma 381, 114736.

Mello, D., Demattê, J.A.M., Silvero, N.E.Q., Di Raimo, L.A.D.L., Poppiel, R.R., Mello, F.A.O., Souza, A.B., Safanelli, J.L., Resende, M.E.B., Rizzo, R., 2020. Soil magnetic susceptibility and its relationship with naturally occurring processes and soil attributes in pedosphere, in a tropical environment. Geoderma 372, 114364. https://doi.org/10.1016/j.geoderma.2020.114364.

Mello, D., Osório Ferreira, T., Vieira Veloso, G., Guedes de Lana, M., Alcantara de Oliveira Mello, F., Augusto Di Loreto Di Raimo, L., Ernesto Gonçalves Reynaud Schaefer, C., Rocha Francelino, M., Inácio Fernandes-Filho, E., Demattê, J.A.M., 2022. Pedogenetic processes operating at different intensities inferred by geophysical sensors and machine learning algorithms. Catena 216, 106370.

Mello, D.C.d., Veloso, G.V., Lana, M.G.d., Mello, F.A.d.O., Poppiel, R.R., Cabrero, D.R.O., Di Raimo, L.A.D.L., Schaefer, C.E.G.R., Filho, E.I.F., Leite, E.P., Demattê, J.A.M., 2022b. A new methodological framework for geophysical sensor combinations associated with machine learning algorithms to understand soil attributes. Geosci. Model Dev. 15 (3), 1219–1246.

Migoń, P., 2013a. Weathering and hillslope development. John F. Schroder (ed.), Treatise Geomorphol. Vol. 4, 159–178.

Migoń, P., 2013b. Weathering mantles and long-term landform evolution. John F. Schroder (ed.), Treatise Geomorphol. 4, 127–144.

Mol, L., Clarke, L., 2019. Integrating structure-from-motion photogrammetry into rock weathering field methodologies. Earth Surf. Process. Landforms 44 (13), 2671–2684.

Mullins, C.E., 1977. Magnetic susceptibility of the soil and its significance in soil science – a review. J. Soil Sci. 28, 223–246. https://doi.org/10.1111/j.1365-2389.1977.tb02232.x.

Nahon, D.B., 1991. Introduction to the petrology of soils and chemical weathering. John Wiley and Sons Inc.

Neogi, S., Dauwels, J., 2019. Factored Latent-Dynamic Conditional Random Fields for Single and Multi-label Sequence Modeling. arXiv Prepr. arXiv1911.03667.

Parshin, A.V., Morozov, V.A., Blinov, A.V., Kosterev, A.N., Budyak, A.E., 2018. Low-altitude geophysical magnetic prospecting based on multirotor UAV as a promising replacement for traditional ground survey. Geo-spatial Inf. Sci. 21 (1), 67–74.

Passier, H.F., de Lange, G.J., Dekkers, M.J., 2001. Magnetic properties and geochemistry of the active oxidation front and the youngest sapropel in the eastern Mediterranean Sea. Geophys. J. Int. 145 (3), 604–614.

Prasetyo, B.H., Suharta, N., Hikmatullah, H., 2016. Chemical and mineralogical properties of ultisols of Sasamba Area, East Kalimantan. Indones. J. Agric. Sci. 2, 37. https://doi.org/10.21082/ijas.v2n2.2001.p37-47.

Price, J.R., Velbel, M.A., 2003. Chemical weathering indices applied to weathering profiles developed on heterogeneous felsic metamorphic parent rocks. Chem. Geol. 202 (3-4), 397–416.

Pride, D.E., Cox, C.A., Moody, S.V., Conelea, R.R., Rosen, M.A., 1990. Investigation of mineralization in the South Shetland Islands, Gerlache Strait, and Anvers Island, northern Antarctic Peninsula. Miner. Resour. Potential Antarct. 51, 69–94.

Pye, K., 1986. Mineralogical and textural controls on the weathering of granitoid rocks. Catena 13, 47–57. https://doi.org/10.1016/S0341-8162(86)80004-2.

R Core Team, 2015. R: A Language and Environment for Statistical Computing. R Foundation for Statistical Computing, Vienna, Austria.

R Core Team, 2022. R: A language and environment for statistical computing.

Rakusa-Suszczewski, S., Mietus, M., Piasecki, J., 1993. Weather and climate. Marit. Antarct. Coast. Ecosyst. Admir. Bay. Warsaw Polish Acad. Sci. 19–25.

Reinhardt, N., Herrmann, L., 2019. Gamma-ray spectrometry as versatile tool in soil science: a critical review. J. Plant Nutr. Soil Sci. 182, 9–27. https://doi.org/10.1002/jpln.201700447.

Rochette, P., Jackson, M., Aubourg, C., 1992. Rock magnetism andn the interpretation of magnetic susceptibility. Rev. Geophys. 30, 209–226.

Rogers, J.J.W., Ragland, P.C., 1961. Variation of thorium and uranium in selected granitic rocks. Geochim. Cosmochim. Acta 25, 99–109. https://doi.org/10.1016/0016-7037(61)90127-2.

Ruiz-Pereira, S., Beriain, E., Cabré, A., Cid-Agüero, P., 2022. Assessment of physical weathering in bedrock areas at the Trinity Peninsula, Antarctica: Towards a

classification of the current weathering grade in polar areas. J. South Am. Earth Sci. 118, 103913.

Rytky, S.J.O., Tiulpin, A., Frondelius, T., Finnilä, M.A.J., Karhula, S.S., Leino, J., Pritzker, K.P.H., Valkealahti, M., Lehenkari, P., Joukainen, A., Kröger, H., Nieminen, H.J., Saarakkala, S., 2020. Automating three-dimensional osteoarthritis histopathological grading of human osteochondral tissue using machine learning on contrast-enhanced micro-computed tomography. Osteoarthr. Cartil. 28, 1133–1144. https://doi.org/10.1016/j.joca.2020.05.002.

Santos, J., Le, E., Souza, C., Oliveira, D., Severino, V., Júnior, D.S., Araújo, F.D., Metri, M., Carlos, A., Azevedo, D., 2019. Geoderma Impact of weathering on REE distribution in soil-saprolite pro fi les developed on orthogneisses in Borborema Province, NE Brazil. Geoderma 347, 103–117. https://doi.org/10.1016/j.geoderma.2019.03.040.

Sarmast, M., Farpoor, M.H., Esfandiarpour Boroujeni, I., 2017. Magnetic susceptibility of soils along a lithotoposequence in southeast Iran. Catena 156, 252–262. https://doi.org/10.1016/j.catena.2017.04.019.

Sasaki, Y., 2007. The truth of the F-measure.

Scarciglia, F., Le Pera, E., Vecchio, G., Critelli, S., 2005. The interplay of geomorphic processes and soil development in an upland environment, Calabria, South Italy. Geomorphology 69, 169–190. https://doi.org/10.1016/j.geomorph.2005.01.003.

Schaefer, C.E.G.R., Pereira, T.T.C., Almeida, I.C.C., Michel, R.F.M., Corrêa, G.R., Figueiredo, L.P.S., Ker, J.C., 2017. Penguin activity modify the thermal regime of active layer in Antarctica: a case study from Hope Bay. Catena 149, 582–591.

Schuler, U., Erbe, P., Zarei, M., Rangubpit, W., Surinkum, A., Stahr, K., Herrmann, L., 2011. A gamma-ray spectrometry approach to field separation of illuviation-type WRB reference soil groups in northern Thailand. J. Plant Nutr. Soil Sci. 174, 536–544. https://doi.org/10.1002/jpln.200800323.

Schwertmann, U., 1988. Occurrence and formation of iron oxides in various pedoenvironments. Iron soils clay Miner. 267–308 https://doi.org/10.1007/978-94-009-4007-9_11.

Seasholtz, M.B., Kowalski, B., 1993. The parsimony principle applied to multivariate calibration. Anal. Chim. Acta 277 (2), 165–177.

Shobe, C.M., Hancock, G.S., Eppes, M.C., Small, E.E., 2017. Field evidence for the influence of weathering on rock erodibility and channel form in bedrock rivers. Earth Surf. Process. Landforms 42 (13), 1997–2012.

Siegert, M., Atkinson, A., Banwell, A., Brandon, M., Convey, P., Davies, B., Downie, R., Edwards, T., Hubbard, B., Marshall, G., 2019. The Antarctic Peninsula under a 1.5° C global warming scenario. What change is it locked into?.

Simas, F.N.B., Schaefer, C.E.G.R., Melo, V.F., Guerra, M.B.B., Saunders, M., Gilkes, R.J., 2006. Clay-sized minerals in permafrost-affected soils (Cryosols) from King George Island, Antarctica. Clays Clay Miner. 54 (6), 721–736.

Simas, F.N.B., Schaefer, C.E.G.R., Filho, M.R.A., Francelino, M.R., Filho, E.I.F., da Costa, L.M., 2008. Genesis, properties and classification of Cryosols from Admiralty Bay, maritime Antarctica. Geoderma 144 (1-2), 116–122.

Siqueira, R.G., Schaefer, C.E.G.R., Fernandes Filho, E.I., Corrêa, G.R., Francelino, M.R., de Souza, J.J.L.L., de Rocha, P., A.,, 2021. Weathering and pedogenesis of sediments and basaltic rocks on Vega Island, Antarctic Peninsula. Geoderma 382, 114707. https://doi.org/10.1016/j.geoderma.2020.114707.

Solutions, R., 2009. Spectrum stabilization and calibration for the RSI RS-125 and RS-230 handheld spectrometers.

Su, Q., Tao, W., Mei, S., Zhang, X., Li, K., Su, X., Guo, J., Yang, Y., 2021. Landslide susceptibility zoning using C5. 0 decision tree, random forest, support vector machine and comparison of their performance in a coal mine area. Front. Earth Sci. 9, 781472.

Tanyu, B.F., Abbaspour, A., Alimohammadlou, Y., Tecuci, G., 2021. Landslide susceptibility analyses using Random Forest, C4.5, and C5.0 with balanced and unbalanced datasets. Catena 203, 105355. https://doi.org/10.1016/j.catena.2021.105355.

Taylor, M.J., Smettem, K., Pracilio, G., Verboom, W., 2002. Relationships between soil properties and high-resolution radiometrics, central eastern Wheatbelt, Western Australia. Explor. Geophys. 33 (2), 95–102.

Teixeira, W., Fairchild, T.R., Toledo, M.C.M. de, Taioli, F., 2009. Decifrando a terra.

Torres, M.A., West, A.J., Clark, K.E., Paris, G., Bouchez, J., Ponton, C., Feakins, S.J., Galy, V., Adkins, J.F., 2016. The acid and alkalinity budgets of weathering in the Andes-Amazon system: Insights into the erosional control of global biogeochemical cycles. Earth Planet. Sci. Lett. 450, 381–391. https://doi.org/10.1016/j.epsl.2016.06.012.

Turkington, A.V., Phillips, J.D., Campbell, S.W., 2005. Weathering and landscape evolution. Geomorphology 67, 1–6. https://doi.org/10.1016/j.geomorph.2004.08.013.

Valaee, M., Ayoubi, S., Khormali, F., Lu, S.G., Karimzadeh, H.R., 2016. Using magnetic susceptibility to discriminate between soil moisture regimes in selected loess and loess-like soils in northern Iran. J. Appl. Geophys. 127, 23–30. https://doi.org/10.1016/j.jappgeo.2016.02.006.

Vicca, S., Goll, D.S., Hagens, M., Hartmann, J., Janssens, I.A., Neubeck, A., Peñuelas, J., Poblador, S., Rijnders, J., Sardans, J., Struyf, E., Swoboda, P., Groenigen, J.W., Vienne, A., Verbruggen, E., 2022. Is the climate change mitigation effect of enhanced silicate weathering governed by biological processes? Glob. Chang. Biol. 28 (3), 711–726.

Viles, H., Goudie, A., Grab, S., Lalley, J., 2011. The use of the Schmidt Hammer and Equotip for rock hardness assessment in geomorphology and heritage science: a comparative analysis. Earth Surf. Process. landforms 36 (3), 320–333.

Walder, J., Hallet, B., 1985. A theoretical model of the fracture of rock during freezing. Geol. Soc. Am. Bull. 96, 336–346.

White, W.M., 2018. Encyclopedia of Geochemistry: A Comprehensive Reference Source on the Chemistry of the Earth. Springer International Publishing.

Wilford, J., 2012. A weathering intensity index for the Australian continent using airborne gamma-ray spectrometry and digital terrain analysis. Geoderma 183–184, 124–142. https://doi.org/10.1016/j.geoderma.2010.12.022.

Wilford, J., Minty, B., 2006. Chapter 16 The Use of Airborne Gamma-ray Imagery for Mapping Soils and Understanding Landscape Processes. Dev. Soil Sci. 31. https://doi.org/10.1016/S0166-2481(06)31016-1.

Wilford, J.R., Bierwirth, P.N., Craig, M.A., 1997. Application of airborne gamma-ray spectrometry in soil/regolith mapping and applied geomorphology. AGSO J. Aust. Geol. Geophys. 17, 201–216.

Wilford, J.R., Searle, R., Thomas, M., Pagendam, D., Grundy, M.J., 2016. A regolith depth map of the Australian continent. Geoderma 266, 1–13. https://doi.org/10.1016/j.geoderma.2015.11.033.

Wilford, J., Thomas, M., 2012. Modelling soil-regolith thickness in complex weathered landscapes of the central Mt Lofty Ranges. South Australia.

Xing, J., Wang, S.X., Jang, C., Zhu, Y., Hao, J.M., 2011. Nonlinear response of ozone to precursor emission changes in China: a modeling study using response surface methodology. Atmos. Chem. Phys. 11, 5027–5044.

Xu, X., Li, W., Tao, M., Xie, Z., Gao, X., Yue, L., Wang, P., 2020. Effective and Accurate Diagnosis of Subjective Cognitive Decline Based on Functional Connection and Graph Theory View. Front. Neurosci. 14.

Yoo, K., Mudd, S.M., Sanderman, J., Amundson, R., Blum, A., 2009. Spatial patterns and controls of soil chemical weathering rates along a transient hillslope. Earth Planet. Sci. Lett. 288, 184–193. https://doi.org/10.1016/j.epsl.2009.09.021.

Yu, C., Peng, B., Peltola, P., Tang, X., Xie, S., 2012. Effect of weathering on abundance and release of potentially toxic elements in soils developed on Lower Cambrian black shales, P. R. China. Environ. Geochem. Health 34, 375–390. https://doi.org/10.1007/s10653-011-9398-y.